batteries

MDPI

Article

MXene Film/Foam Bilayer Anodes with Enhanced Electrochemical Performance for Self-Standing Lithium-Ion Batteries

Tae Hyeon Park †, Ki Yun Kim † and Jea Uk Lee *

Department of Materials Science and Engineering, Kyung Hee University, Yongin-si 17104, Gyeonggi-do, Republic of Korea; pth122133@khu.ac.kr (T.H.P.); 12rldbs@khu.ac.kr (K.Y.K.)

* Correspondence: leeju@khu.ac.kr; Tel.: +82-31-201-3655

† These authors contributed equally to this work.

Abstract

The structural design of self-standing electrodes without binders and current collectors is critical for maximizing the energy density of lithium-ion batteries, yet achieving electrical conductivity, ion accessibility, and mechanical integrity in a single architecture remains challenging. Although $Ti_3C_2T_x$ MXene is a promising candidate, owing to its high metallic conductivity and structural robustness, conventional dense films suffer from restacking-induced restricted electrolyte penetration and Li^+ diffusion. Conversely, porous MXene foams can mitigate restacking but exhibit weak electrical contact and limited mechanical robustness. To overcome this structural trade-off, we designed a self-standing MXene film/foam bilayer anode integrating a compact film layer with a porous foam layer, which was followed by air annealing to generate TiO_2/TiO_x-containing active sites. Among the various film/foam ratios systematically evaluated, the optimal 2:8 bilayer electrode exhibited low charge-transfer resistance and fast redox kinetics, delivering 83.24 mAh g^{-1} at 1000 mA g^{-1} and retaining 195.12 mAh g^{-1} at 50 mA g^{-1} after 200 cycles, outperforming the single-architecture electrodes. These results demonstrate that the bilayer design effectively combines the structural and electrical stability of the film with the rapid ion transport and abundant active sites of the foam, offering a promising strategy for high-performance self-standing anodes.

Keywords: MXene; self-standing electrode; film/foam bilayer; lithium-ion battery

1. Introduction

Lithium-ion batteries (LIBs) are widely used in portable electronic devices, electric vehicles, and energy storage systems owing to their high energy density, long cycle life, and stable operation [1–4]. Recently, the growing demand for wearable electronics, flexible devices, and lightweight energy storage systems has stimulated extensive research into self-standing electrodes that can replace conventional electrode architectures based on metallic current collectors, polymer binders, and conductive additives. Self-standing electrodes are advantageous for reducing cell weight and improving energy density because they minimize the use of electrochemically inactive components while increasing the fraction of active materials [5–7]. However, because self-standing electrodes must simultaneously provide sufficient electrical conductivity, mechanical integrity, and efficient ion-transport pathways, the rational structural design of electrode materials plays a critical role in determining their electrochemical performance. Various strategies have been explored to construct self-standing electrodes without metal current collectors, binders, or conductive

Check for updates

Academic Editors: Peng Zuo and Jihyeon Gim

Received: 25 September 2026
Revised: 12 October 2026
Accepted: 14 October 2026
Published: 16 October 2026

Copyright: © 2026 by the authors. Licensee MDPI, Basel, Switzerland. This article is an open access article distributed under the terms and conditions of the Creative Commons Attribution (CC BY) license.

additives, employing carbon- and metal-nanowire-based conductive frameworks combined with active materials such as $Li_4Ti_5O_{12}$, Fe_3O_4, and Si (Table S1) [8–14]. In these architectures, however, the conductive framework itself is typically electrochemically inactive and serves only a structural and conductive role, so the overall capacity is governed by the embedded active material. This limitation highlights the need for self-standing electrodes in which the framework itself can also function as the electrochemically active material, rather than relying on a separately embedded active component.

MXenes are a family of two-dimensional transition metal carbides, nitrides, and carbonitrides, generally represented by the formula $M_{n+1}X_nT_x$ [15–19]. Among them, $Ti_3C_2T_x$ MXene is typically synthesized by selectively etching Al layers from the Ti_3AlC_2 MAX phase and exhibits high electrical conductivity (10^3–10^4 S cm^{-1}), hydrophilic surface terminations (e.g., –O, –OH, –F), excellent solution processability, and mechanical flexibility [20,21]. Owing to these characteristics, $Ti_3C_2T_x$ MXene has attracted considerable attention as a promising self-standing anode material for lithium-ion batteries [22–27]. For example, self-standing MXene films can be readily fabricated by vacuum filtration of aqueous MXene dispersions, and the intimate contact between MXene sheets provides continuous electron transport pathways and structural stability [28]. However, in film-type electrodes, sheet restacking readily occurs during drying and assembly, reducing interlayer spacing and restricting electrolyte penetration and Li^+ diffusion [29]. Consequently, despite their favorable electron transport and structural stability, MXene films may suffer from limited Li^+ storage space and insufficient utilization of electrochemically active surface areas.

To mitigate this restacking issue, self-standing porous MXene foam electrode architectures have been proposed as an effective alternative [30,31]. Porous MXene foam electrodes can facilitate electrolyte penetration and provide continuous Li^+ diffusion pathways by forming open pores and interconnected channels between MXene sheets [32,33]. However, compared with compact film structures, foam architectures generally exhibit weaker intersheet contact and reduced continuity of the electron transport network [34]. Moreover, interfacial instability associated with high specific surface area and limited mechanical robustness can induce pore-wall collapse and crack propagation during long-term cycling, ultimately compromising structural durability [35]. The structural characteristics of these MXene film and foam architectures are schematically illustrated in Figure 1.

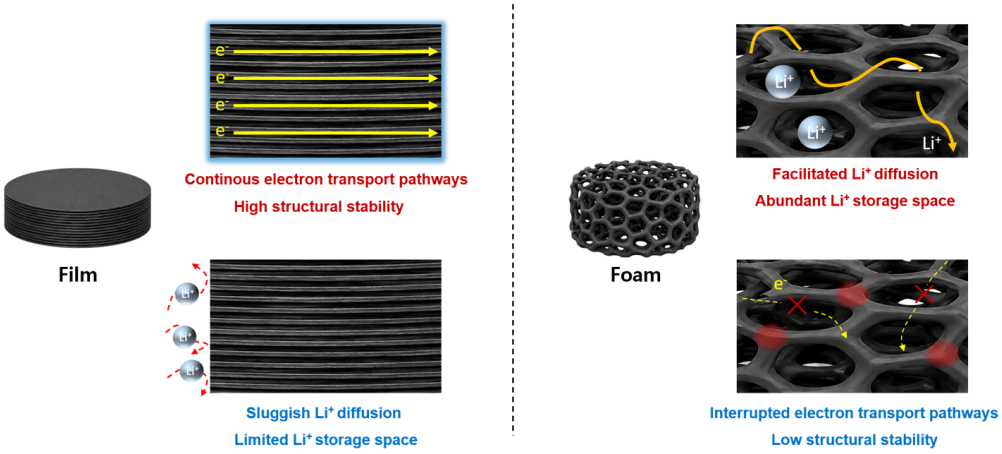


Figure 1. Schematic illustration of the structural formation of compact MXene film and porous MXene foam electrodes.

In this study, we designed a self-standing film/foam bilayer anode by integrating a compact film layer with a porous foam layer based on $Ti_3C_2T_x$ MXene, selected for its high electrical conductivity and hydrophilic surface terminations. This anode-focused

design leverages the redox behavior of $Ti_3C_2T_x$ MXene and its surface oxidation products (TiO_2/TiO_x), which operate within the low-voltage, reductive potential window characteristic of anode materials. In this design, the two layers have distinct functional roles: the bottom film layer serves as a robust conductive backbone that ensures continuous electron pathways and mechanical stability, whereas the top porous foam layer facilitates rapid electrolyte infiltration and unhindered Li^+ diffusion. In addition, annealing in an air atmosphere at 300 °C was employed to remove the sulfur template and form the porous foam layer; this annealing process also induced controlled oxidation of the MXene surface, thereby generating TiO_2/TiOx-containing active surfaces that can provide additional Li^+ storage sites. Based on this design, the structural characteristics, surface chemistry, wettability, electrochemical kinetics, and cycling stability of pure film, pure foam, and bilayer electrodes with different film/foam ratios were systematically compared. Among the evaluated configurations, the optimal MXene film:foam 2:8 bilayer electrode exhibited the most balanced combination of electrical connectivity, structural integrity, and effective Li^+ diffusion, resulting in stable charge transport kinetics, improved rate capability, and long-term cycling performance over 200 cycles. This study presents a bilayer electrode design strategy that simultaneously addresses the restacking limitation of MXene films and the structural instability of MXene foams, providing a promising pathway for developing high-performance self-standing lithium-ion battery anodes [36–41].

2. Materials and Methods

2.1. Materials

Titanium aluminum carbide (Ti_3AlC_2, MAX) was purchased from innoMXene (Seoul, Republic of Korea). Lithium fluoride (LiF) was purchased from Fujifilm (Tokyo, Japan). Sodium hydroxide (NaOH, pellets, 98.0%) and sodium thiosulfate pentahydrate ($Na_2S_2O_3 \cdot 5H_2O$, 98.5%) were purchased from Samchun Chemical Co., Ltd. (Seoul, Republic of Korea). Hydrochloric acid (HCl, 36.0%) was purchased from Kanto Chemical Co., Inc. (Tokyo, Japan). Polyvinylpyrrolidone (PVP) was purchased from Sigma-Aldrich (St.Louis, MO, USA). All chemicals were used as received without further purification.

2.2. Synthesis of $Ti_3C_2T_x$ MXene

$Ti_3C_2T_x$ MXene was synthesized from the Ti_3AlC_2 MAX phase using a LiF/HCl etching method [42]. Briefly, 3.0 g of LiF was dissolved in 60 mL of 36% HCl solution under stirring to prepare the etching solution. Subsequently, 3.0 g of Ti_3AlC_2 powder was slowly added to the etching solution, and the mixture was continuously stirred at 50 °C for 24 h to selectively etch the Al layers. After etching, the suspension was repeatedly washed by centrifugation with deionized water until the supernatant reached a near-neutral pH. The obtained sediment was redispersed in deionized water and sonicated for 20 min, followed by two cycles of vortex mixing for 10 min to facilitate delamination of the MXene sheets. The resulting $Ti_3C_2T_x$ MXene dispersion was collected and used to fabricate film, foam, and bilayer electrodes.

2.3. Fabrication of MXene Film, Foam, and Bilayer Electrodes

MXene film electrodes were prepared by vacuum-filtrating the $Ti_3C_2T_x$ MXene aqueous dispersion. During filtration, MXene sheets were stacked into a compact lamellar structure, forming a self-standing MXene film after drying. The resulting MXene film electrodes were annealed in an air atmosphere at 300 °C for 3 h under the same conditions used for the foam and bilayer electrodes to induce partial surface oxidation while maintaining the compact MXene framework.

MXene foam electrodes were fabricated using sulfur particles as a sacrificial template [32]. Specifically, 100 g of $Na_2S_2O_3 \cdot 5H_2O$ and 0.012 g of PVP were dissolved in 1000 mL of deionized water. Sulfur particles were then generated by the dropwise addition of HCl (3 mol L^{-1}, 20% in excess of the stoichiometric amount), and the reaction was terminated and neutralized by adding NaOH solution (2 mol L^{-1}). The $Ti_3C_2T_x$ MXene dispersion (12.56 mg of MXene) was then added to 64 mL of the resulting sulfur suspension under stirring, corresponding to a sulfur content of 71.0% in the MXene/sulfur film. The resulting suspension was vacuum-filtered to form a self-standing electrode, which was dried at room temperature under vacuum. The dried electrode was then annealed in an air atmosphere at 300 °C (5 °C min^{-1}) for 3 h, during which the sacrificial sulfur templates were removed, resulting in the formation of an interconnected porous MXene foam structure.

MXene film/foam bilayer electrodes were fabricated by sequential vacuum filtration of the MXene dispersion and the MXene/sulfur-template mixture. The mass ratio of the film layer to the foam layer was controlled by vacuum-filtering a calculated volume of each dispersion, based on its known MXene concentration, to prepare 1:9, 2:8, and 3:7 bilayer electrodes. After filtration, the obtained bilayer electrodes were dried and annealed in an air atmosphere at 300 °C for 3 h. The resulting electrodes were denoted as pure film, pure foam, 1:9 bilayer, 2:8 bilayer, and 3:7 bilayer according to their structural composition. Film fractions were limited to $\leq$30% because the film layer was designed to function as a current-collecting, electron-conducting backbone rather than as a Li^+-storage-active component. Further details of the fabrication process are provided in Figure S1, which includes a schematic illustration together with photographs of the synthesized MXene dispersion and the fabricated film, foam, and bilayer electrodes.

2.4. Materials Characterization

Surface and cross-sectional morphologies were observed by scanning electron microscopy (SEM, Merlin, Zeiss, Oberkochen, Germany). The specific surface area and pore characteristics of the film and foam electrodes were evaluated by nitrogen adsorption–desorption measurements at 77 K employing a surface area and porosity analyzer (Tristar 2, Micromeritics, Norcross, GA, USA). The specific surface area was calculated using the Brunauer–Emmett–Teller (BET) method [43]. Contact angle measurements (CA, Phoenix 300, SEO Co., Ltd., Suwon, Republic of Korea) were performed using deionized water to evaluate electrolyte wettability, as the electrolyte itself wetted the electrode surfaces too rapidly for a measurable contact angle to evaluate electrolyte wettability (Figure S2). X-ray diffraction (XRD, D8 Advance, Bruker, Karlsruhe, Germany) was used to analyze the crystal structures at a scan rate of 5° min^{-1} using Cu Kα radiation (λ = 1.5406 Å). Quantitative phase analysis of the anatase and rutile TiO_2 phases was performed by Rietveld refinement (Profex/BGMN) restricted to the anatase (101) and rutile (110) reflections (2θ = 22–31°). X-ray photoelectron spectroscopy (XPS, K-Alpha, Thermo Fisher Scientific, Waltham, MA, USA) was used to analyze the surface chemical composition and oxidation states of the electrodes.

2.5. Electrochemical Measurements

The MXene film, foam, and bilayer electrodes were directly used as self-standing anodes. The electrodes were punched into circular disks with a diameter of 14 mm, corresponding to an electrode area of 1.5394 cm^2. The electrode loading was controlled at approximately 1.0–1.5 mg cm^{-2}. Coin-type half cells (CR2032) were assembled in an Ar-filled glove box with oxygen and moisture levels below 1 ppm. The prepared electrodes were used as the working electrodes, lithium metal was used as both the counter and

reference electrode, and glass fiber (GF5-025, CHMLAB GROUP, Spain) was used as the separator. The electrolyte consisted of 1 M $LiPF_6$ dissolved in a mixed solvent of ethylene carbonate (EC), diethyl carbonate (DEC), and ethyl methyl carbonate (EMC) with a volume ratio of 1:1:1, with 5 vol% fluoroethylene carbonate (FEC) as an additive. Galvanostatic charge–discharge tests were conducted in the voltage range of 0.01–2.5 V (vs. Li/Li^+) at room temperature using a multichannel battery tester (WHW-200L-0C-220V-9U, Neware, Shenzhen, China) [44]. Cyclic voltammetry (CV, WBCS3000Le32, WonATech, Seoul, Republic of Korea) measurements were performed over a voltage range of 0.01–1 V at scan rates of 0.1–2 mV s^{-1} [34]. Electrochemical impedance spectroscopy (EIS) measurements were performed using a potentiostat (ZIVE SP1 system, WonATech, Seoul, Republic of Korea) with an AC amplitude of 10 mV over a frequency range from 10^5 to 10^{-2} Hz [45]. Electrochemical reproducibility of rate capability and cycling performance was evaluated using five independently assembled cells (n = 5) for each electrode configuration, and the data are presented as mean ± standard deviation (SD).

3. Results and Discussion

3.1. Design and Fabrication of MXene Film/Foam Bilayer Electrodes

Figure 2 illustrates the structural design rationale of the MXene film, foam, and bilayer electrodes. Based on the two-dimensional sheet structure of $Ti_3C_2T_x$ MXene, compact film and porous foam architectures were individually constructed and subsequently integrated into a self-standing bilayer electrode. The MXene film was prepared by vacuum filtration of an aqueous MXene dispersion, during which MXene sheets were aligned and restacked into a compact lamellar structure, as confirmed by the cross-sectional SEM images in Section 3.2 (Figure 3d–f). This film architecture exhibits extensive inter-sheet contact, thereby providing continuous electron transport pathways and improving the mechanical integrity of the electrode. However, such dense stacking reduces the interlayer spacing and consequently restricts electrolyte penetration and Li^+ diffusion [34]. MXene foam was fabricated using sulfur particles as a sacrificial template. Following the incorporation of sulfur particles between the MXene sheets, the sacrificial template was removed via thermal treatment in an air atmosphere, resulting in the formation of interconnected porous channels within the electrode. This foam architecture provides sufficient space for electrolyte infiltration and facilitates Li^+ transport through shortened diffusion pathways. However, excessive porosity can reduce inter-sheet contact and weaken the continuity of the electron transport network, potentially leading to pore collapse or structural discontinuity during long-term cycling [35].

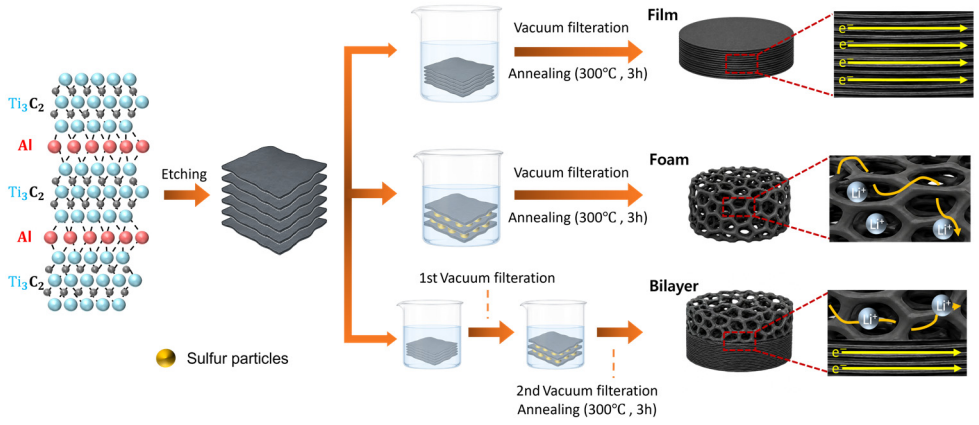


Figure 2. Schematic illustration of the fabrication and structural design of self-standing MXene film, foam, and bilayer electrodes, highlighting the continuous electron transport pathways in the film layer and the facilitated Li^+ diffusion channels in the foam layer.

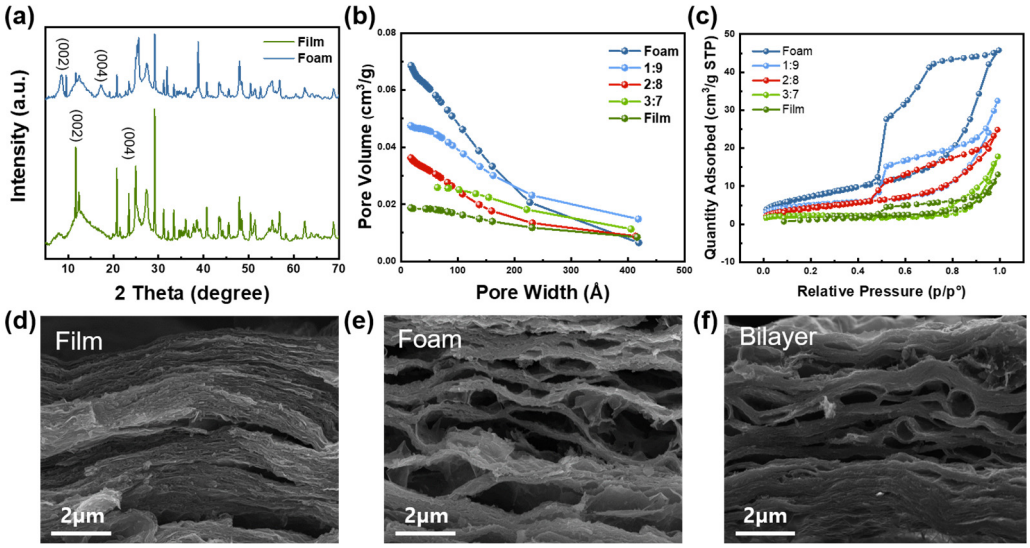


Figure 3. Structural characterization of MXene film, foam, and bilayer electrodes. (**a**) XRD patterns; (**b**) pore size distributions; (**c**) N_2 adsorption–desorption isotherms; (**d**–**f**) cross-sectional SEM images of the electrodes.

To exploit the complementary characteristics of the film and foam structures, an MXene bilayer electrode was designed by sequentially vacuum-filtering a film layer and a foam layer, allowing the foam layer to serve as the outer, electrolyte-contacting surface of the electrode. In this configuration, the functional roles are spatially separated: the bottom film layer serves as a continuous electron transport pathway and mechanical support, whereas the exposed top foam layer provides open channels for facile electrolyte infiltration and rapid Li^+ diffusion.

3.2. Structural Characterization of MXene Film, Foam, and Bilayer Electrodes

Figure 3 compares the crystal structure, pore characteristics, and cross-sectional morphology of the MXene film, foam, and bilayer electrodes. In the XRD patterns shown in Figure 3a, both the film and foam electrodes exhibited low-angle diffraction peaks associated with the layered structure of $Ti_3C_2T_x$ MXene. In general, the characteristic (002) reflection of $Ti_3C_2T_x$ MXene is a key indicator of the layered MXene structure formed after removal of the Al layer, typically observed in the low-angle region of approximately $2\theta = 6–9°$, depending on the interlayer spacing between MXene sheets [32]. For the film electrode, a distinct peak appeared at $2\theta = 11.69°$, corresponding to a d-spacing of approximately 7.56 Å. This peak position is located at a higher angle than the typical (002) reflection of hydrated MXene, indicating reduced interlayer spacing caused by the compact restacking of the film structure. In contrast, the foam electrode exhibited multiple low-angle peaks at 8.53°, 9.59°, 11.72°, and 12.44°, corresponding to d-spacings of approximately 10.35, 9.22, 7.55, and 7.11 Å, respectively. The additional low-angle peaks at 8.53° and 9.59° in the foam electrode, compared with the film electrode, indicate that significant restacking of MXene sheets was suppressed during the introduction and removal of the sulfur template, resulting in porous MXene domains with expanded interlayer spacing [35]. In addition, characteristic diffraction peaks corresponding to anatase and rutile TiO2 were observed in both electrodes (e.g., anatase (101) at ~25.5–26.0° and rutile (110) at ~27.4–27.5°) [46], confirming that surface Ti species partially oxidized into TiO_2/TiO_x active phases during the 300 °C air annealing [47]. To quantify the relative proportions of these two TiO_2 polymorphs, Rietveld refinement of the anatase (101) and rutile (110) reflections yielded anatase:rutile weight fractions of 86.2:13.8 and 88.5:11.5 for the film and foam electrodes, respectively, consistent with both electrodes having undergone the same thermal anneal-

ing treatment (Table S2). Taken together, the XRD results clearly confirm that while the film electrode forms a densely restacked lamellar network, the sacrificial templating effectively preserves an expanded interlayer spacing in the foam structure, along with in situ-generated TiO_2/TiO_x active sites.

Figure 3b,c present the pore size distributions and nitrogen adsorption–desorption isotherms of the electrodes. The film electrode exhibited a relatively low total pore volume of 0.0202 $cm^3\ g^{-1}$ and BET surface area of 6.31 $m^2\ g^{-1}$, reflecting the densely stacked MXene sheet structure. In contrast, the foam electrode exhibited a pronounced increase in total pore volume to 0.0708 $cm^3\ g^{-1}$ and BET surface area of 26.55 $m^2\ g^{-1}$, particularly in the mesopore region up to approximately 200 Å, indicating that abundant pores were formed between the MXene sheets following the removal of the sulfur template. The higher N_2 uptake and distinct hysteresis further demonstrate the formation of a mesoporous and interconnected channel network [32]. This foam structure provides additional space for electrolyte infiltration, thereby facilitating Li^+ diffusion. The pore characteristics of the bilayer electrodes exhibited a systematic dependence on the film/foam ratio, indicating that the porosity of the bilayer structure can be tuned by adjusting this ratio.

Figure 3d–f show cross-sectional SEM images that directly reveal the structural differences among the film, foam, and bilayer electrodes. The film electrode exhibits a densely stacked lamellar structure composed of MXene sheets with a thickness of approximately 8–10 μm. Consistent with this compact structure, the film electrode and the film-side plane of the 2:8 bilayer exhibited higher electrical conductivity (3096.45 and 1970.06 S/m) than their foam counterparts (686.86 and 569.22 S/m) (Table S3), further supporting the role of the film layer as an electron transport pathway. In contrast, the foam electrode displays a porous architecture with relatively large open pores and interconnected channels and a thickness of approximately 14–16 μm, providing a morphology facilitating electrolyte infiltration and Li^+ transport [34]. In the bilayer electrode, the compact film layer and porous foam layer are simultaneously observed within a single electrode (approximately 10–14 μm in total thickness for the 1:9, 2:8, and 3:7 electrodes). This confirms the successful integration of the intended bilayer architecture, in which the two layers cooperate to provide structural stability, electron transport, and Li^+ diffusion. Furthermore, the EDS elemental mapping images show the homogeneous distribution of C, O, and Ti throughout the film, foam, and bilayer electrodes (Figure S3), confirming that the MXene-based electrode structures were uniformly formed without severe elemental segregation.

3.3. Wettability and Surface Chemistry of Partially Oxidized MXene Electrodes

Figure 4 compares the electrolyte wettability and surface chemical states of the MXene film, foam, and bilayer electrodes. Figure 4a–c present the contact angle measurements performed to assess the electrolyte wettability of the film and foam structures. The pure film electrode exhibited a contact angle of approximately 68.7°, whereas the pure foam electrode showed a much lower contact angle of approximately 38.2°. The reduced contact angle of the foam electrode can be attributed to the capillary effect arising from the porous channels and increased surface exposure, indicating that the foam structure provides superior electrolyte wettability compared with the compact film structure [48]. For the bilayer electrodes, the contact angles of the film and foam layers were measured separately to evaluate whether the two layers retained their distinct functional characteristics. In the 1:9 bilayer, the contact angle of the film layer markedly decreased and became comparable to that of the foam layer, suggesting that the film layer did not sufficiently retain film-like wettability and was influenced by the capillary effect of the foam layer. In contrast, the 2:8 bilayer maintained a relatively clear difference in contact angle between the film and foam layers, indicating that the structural integrity required for the electron transport

of the film and the electrolyte infiltration function of the foam could be simultaneously preserved. For the 3:7 bilayer, both layers showed increased contact angles, implying that the overall electrolyte wettability of the electrode may decrease as the film fraction increases. Consequently, in the 2:8 bilayer electrode, each layer effectively preserves its own interfacial characteristics; the superior electrolyte wettability of the top foam layer facilitates rapid Li+ access to active sites, while the dense film base ensures structural support. Therefore, the contact angle results indicate that the 2:8 bilayer provides the most balanced wetting characteristics between the film and foam layers, as further visualized in the representative contact-angle images of each side (Figure S4).

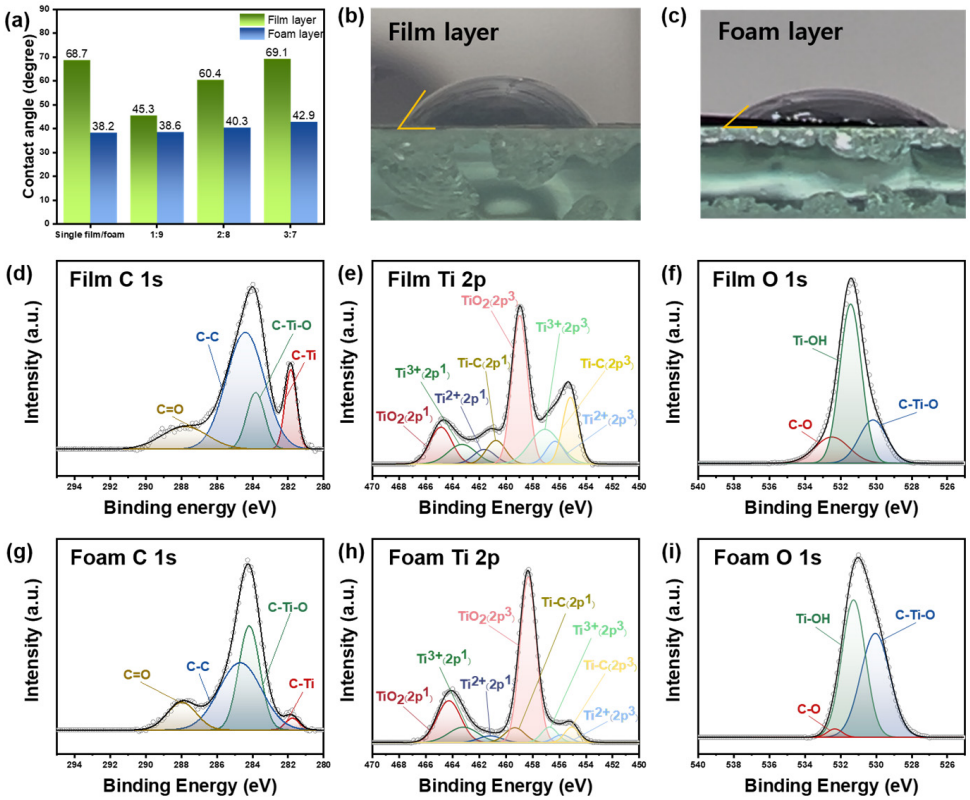


Figure 4. Wettability and surface chemistry of MXene film, foam, and bilayer electrodes. (**a**–**c**) Contact angle results and (**d**–**i**) high-resolution C 1s, Ti 2p, and O 1s XPS spectra of the film and foam electrodes.

Figure 4d–i show the C 1s, Ti 2p, and O 1s XPS spectra of the film and foam electrodes, and the corresponding survey spectra are provided in Figure S5. All XPS spectra were calibrated using the C–C peak of adventitious carbon at 284.8 eV as a reference. In the C 1s spectrum of the film electrode, the components corresponding to C-Ti, C-Ti-O, C-C, and C=O were identified at approximately 281.8, 283.8, 284.8, and 288.5 eV, respectively. Among these, the presence of the C-Ti peak indicates that the conductive carbide framework of $Ti_3C_2T_x$ MXene was substantially retained even after annealing in an air atmosphere at 300 °C [49]. In addition, the formation of the C-Ti-O peak suggests that a portion of the Ti-C bonds on the MXene surface reacted with oxygen, resulting in an oxycarbide or partially oxidized MXene structure. This confirms that the film electrode forms a partially oxidized architecture in which surface oxidation is controlled while maintaining the conductive carbide framework. In the Ti 2p spectrum of the film electrode, characteristic doublets corresponding to Ti–C (~455.0 and 461.0 eV), Ti^{2+} (~456.2 and 462.3 eV), Ti^{3+} (~457.3 and 463.5 eV), and TiO_2 (~458.6 and 464.5 eV) were identified. These results indicate the coexistence of a residual $Ti_3C_2T_x$ framework, intermediate TiO_x species, and TiO_2 phases on the surface of the film electrode. Specifically, the remaining Ti–C component confirms

that the film structure retains the MXene-based electron transport pathway, while the presence of TiO_2 and TiO_x species supports the formation of additional Li^+ storage active sites through controlled oxidation. In the O 1s spectrum of the film electrode, three major components were observed at approximately 530.0, 531.3, and 532.5 eV, corresponding to C-Ti-O, Ti-OH, and C-O, respectively. The presence of these peaks confirms that oxygen-containing functional groups and hydroxyl terminations were formed on the film electrode surface after thermal treatment in air. Notably, this indicates that the partially oxidized surface of the film electrode is not merely an oxidative byproduct, but actively contributes to Li^+ storage by enhancing interfacial reactivity and providing additional active sites for Li^+ adsorption and diffusion [50].

The XPS spectra of the foam electrode exhibited more highly pronounced oxidation features than those of the film electrode. In the C 1s spectrum of the foam electrode, the C-Ti component at approximately 281.8 eV decreased, whereas the C-Ti-O component at approximately 283.8 eV increased (Table S4). This is because the porous foam architecture has a larger exposed surface area, allowing oxygen to readily reach the MXene sheets. In the Ti 2p spectrum of the foam electrode, the TiO_2 component was also distinctly more dominant than in the film electrode. In particular, the TiO_2-related peaks at approximately 458.6 and 464.5 eV showed greater intensity than the Ti-C and lower-valence Ti^{2+}/Ti^{3+} components [46]. These results indicate that the surface Ti species in the foam structure underwent a higher degree of oxidation than those in the compact film structure. In the O 1s spectrum of the foam electrode, distinct components corresponding mainly to C-Ti-O or Ti-O and Ti-OH were observed at approximately 530.0 and 531.3 eV, respectively. This indicates that the foam structure, with its high specific surface area, is more susceptible to forming an oxide-rich surface than the compact film structure, which is further supported by the higher O/Ti ratio observed for the foam electrode compared with the film electrode (Table S5). The relatively high Al and F contents of the foam electrode are likely attributable to residual Al- and F-containing species remaining from the MXene etching and washing process, which are more readily detected on the foam surface owing to its larger exposed surface area. Consequently, these surface-chemical analyses provide direct evidence that the porous foam architecture not only improves interfacial Li^+ transport through enhanced electrolyte affinity but also provides a significantly greater abundance of Li^+ storage active sites via greater TiO_2/TiO_x content compared to the compact film.

Consequently, the contact angle and XPS analyses in Figure 4 demonstrate that both electrode architecture and surface chemistry contribute synergistically to the electrochemical performance. The film structure retains the conductive Ti-C framework to a greater extent, which is advantageous for electron transport and structural stability. In contrast, the foam structure, with a higher degree of oxidation and abundant oxygen-containing functional groups, is beneficial for enhancing electrolyte wettability and interfacial Li^+ transport, as well as providing abundant Li^+ storage sites. By integrating these two complementary features into a single bilayer design, this architecture enables the simultaneous utilization of a conductive MXene framework and an oxide-rich active surface.

3.4. Electrochemical Kinetics and Lithium-Ion Storage Performance

To elucidate the structural advantages of the integrated design, the electrochemical charge-storage kinetics and comprehensive lithium-ion storage performance of the MXene film, foam, and bilayer electrodes were systematically evaluated. Figure 5a–c show the CV curves of the film, foam, and 2:8 bilayer electrodes obtained over 50 cycles at a scan rate of 0.1 mV s^{-1}. Both the film and foam electrodes exhibited markedly smaller current responses than the 2:8 bilayer electrode. For the film electrode, the current density slightly increased with cycling, likely due to gradual electrolyte infiltration into the densely

restacked structure, whereas the foam electrode maintained nearly overlapping CV curves throughout cycling, consistent with rapid electrolyte access through its porous architecture. In contrast, the 2:8 bilayer electrode exhibited a substantially larger enclosed CV area and current response than both single-layer electrodes while maintaining stable, overlapping curves across cycling. This enhancement indicates that the electrolyte-exposed foam layer provides extensive Li^+ accessibility, while the underlying film layer supplies continuous electron transport and structural support, together enabling efficient and stable Li^+ storage. Consequently, the apparent Li^+ diffusion coefficients of the 2:8 bilayer electrode, estimated from the CV data using the Randles–Ševčík equation (Figure S6), were 3.53×10^{-11} and 2.40×10^{-11} cm^2 s^{-1} for the anodic and cathodic processes, respectively, which were higher than those of the film (2.75×10^{-11} and 1.48×10^{-11} cm^2 s^{-1}) and foam (2.74×10^{-11} and 2.15×10^{-11} cm^2 s^{-1}) electrodes. This suggests that the bilayer architecture is favorable for Li^+ transport. Also, the small current features observed near 0.9 V and 0.1 V in Figure 5c are attributed to the current response at the upper and lower vertex potentials of the CV scan window (0.01–1 V) rather than distinct Faradaic redox peaks.

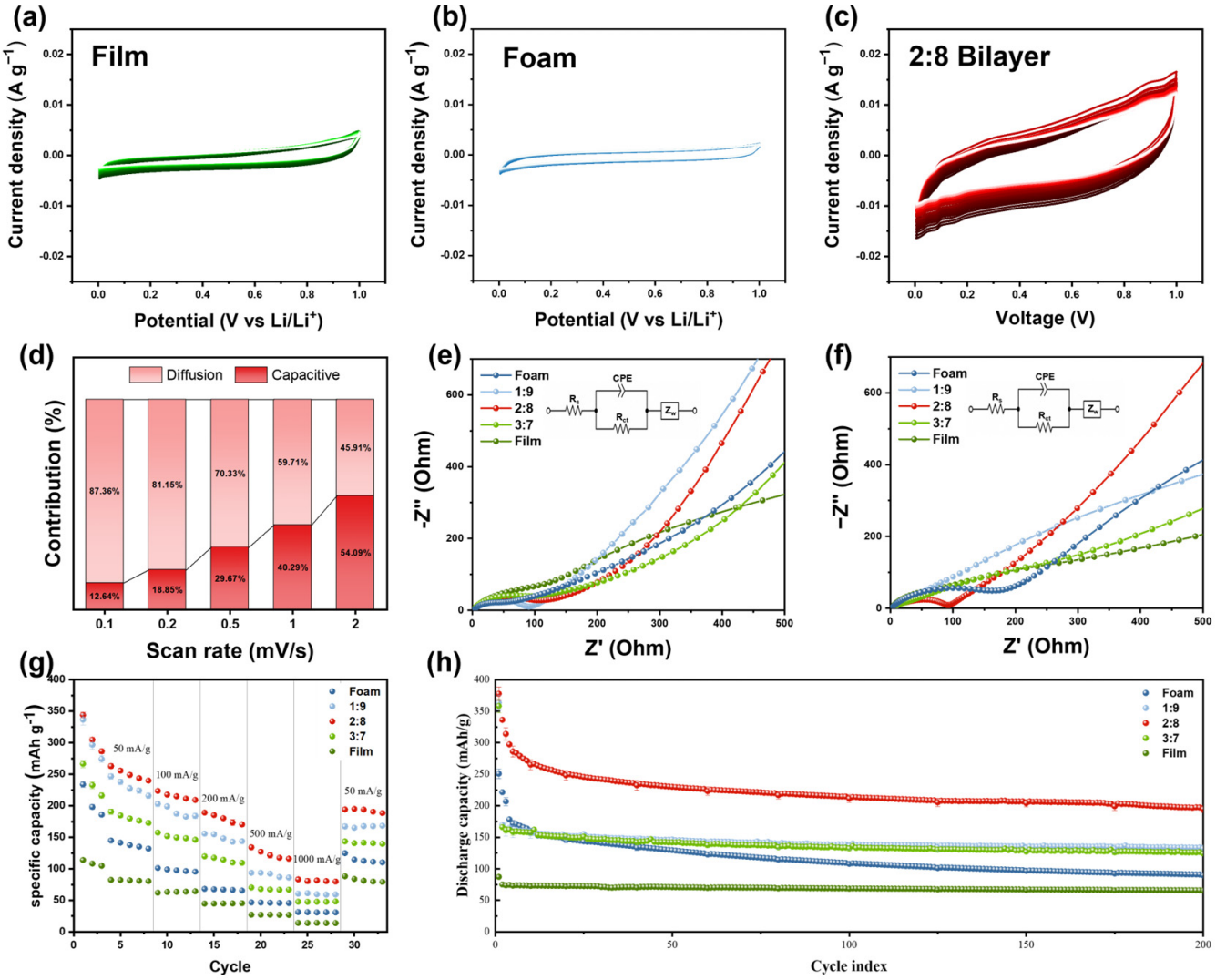


Figure 5. Electrochemical kinetics and Li^+ storage performance of MXene film, foam, and bilayer electrodes. (**a**–**c**) CV curves, (**d**) capacitive and diffusion-controlled contributions, (**e**,**f**) Nyquist plots before and after cycling, (**g**) rate capability and (**h**) cycling performance (mean ± SD, n = 5).

Figures 5d and S7 show the capacitive and diffusion-controlled contributions of the film, foam, and 2:8 bilayer electrodes at different scan rates (0.1–2 mV s^{-1}). In all three electrodes, the capacitive contribution increased progressively with scan rate, consistent with the general kinetic behavior in which faster sweep rates provide insufficient time for Li^+ to diffuse into the bulk electrode, thereby increasing the relative contribution from surface-controlled capacitive processes [51]. The foam electrode showed the highest capacitive contribution among the three electrodes, which can be attributed to the high specific surface area of the foam layer, providing abundant active sites for surface-controlled redox reactions [35]. Furthermore, the capacitive contribution of the bilayer electrode showed a smaller increase (from 12.64% to 54.09%) than that of the film (12.51% to 66.08%) and foam (17.31% to 72.95%) electrodes, suggesting that the diffusion-controlled redox reactions of the bilayer electrode are stably sustained even under fast scan conditions. This restrained increase reflects the synergistic effect of the efficient electron transport from the film layer and the rapid Li^+ diffusion from the foam layer. Together, these complementary pathways successfully sustain bulk Li^+ redox reactions. Consistent with this diffusion-controlled behavior, the peak current also showed a nearly linear relationship with the square root of the scan rate (Figure S6), in agreement with the Randles–Ševčík relationship [52].

Figure 5e,f compare the impedance behavior of the MXene film, foam, and bilayer electrodes before and after 200 cycles using Nyquist plots, while Figure S8 shows the corresponding Nyquist plots after 5 and 30 cycles. In EIS analysis, the high-frequency intercept on the Z' axis corresponds to the series resistance (R_s), which includes electrolyte resistance, intrinsic electrode resistance, and interfacial/contact resistance within the cell. The diameter of the semicircle in the high- to mid-frequency region is associated with the charge-transfer resistance (R_{ct}), which reflects the charge-transfer process involving Li^+ and electron transport at the electrode/electrolyte interface. In addition, the inclined line in the low-frequency region represents Li^+ diffusion behavior within the electrode [53]. Before lithiation, the single-layer film electrode exhibited a larger semicircle than the bilayer electrodes across all film/foam ratios, indicating relatively higher R_{ct} and less favorable charge-transfer kinetics at the electrode/electrolyte interface, whereas the single-layer foam electrode exhibited the smallest semicircle among all samples, reflecting its larger electrolyte-accessible interfacial area. This initial advantage of the foam electrode, however, is not maintained upon extended cycling. Although the film electrode is advantageous for electron transport owing to the intimate contact between MXene sheets, its densely restacked structure restricts electrolyte penetration and reduces the electrochemically active interfacial area, resulting in increased charge-transfer resistance. In contrast, the foam electrode benefits from favorable electrolyte penetration and Li^+ diffusion pathways through its porous architecture, although its weaker inter-sheet contact can compromise the mechanical stability of the porous network, particularly during extended cycling. These results indicate that when film or foam architectures are used as single self-standing electrodes, they suffer from limited charge-transfer kinetics associated with either electron transport or Li^+ transport during long-term cycling. By contrast, the bilayer electrodes exhibited smaller semicircles than the single-layer film electrode, suggesting that the bilayer architecture mitigates the resistance limitation associated with the compact film structure. This improvement can be attributed to the distinct functions of the two layers: the lower film layer provides a continuous electron transport pathway, while the upper foam layer offers efficient Li^+ transport pathways. As a result, both electron and Li^+ transport kinetics are simultaneously improved. Among these, the 2:8 bilayer electrode maintained the most stable charge-transfer resistance throughout cycling, owing to the optimized balance between the conductive network of the film layer and the ion diffusion pathways of the foam layer. After 200 cycles, the film and foam electrodes exhibited relatively large semicircles, suggesting

that both electron and Li^+ transport deteriorated in these single-architecture electrodes; detailed fitting parameters are provided in Table S6. To further clarify the evolution of the impedance parameters during cycling, the fitted R_s and R_{ct} values at 0, 5, 30, and 200 cycles are presented in Figure S9. The R_{ct} of the 2:8 bilayer electrode remained within 61.65–107.09 Ω over 200 cycles (102.29, 107.09, 61.65, and 88.85 Ω at 0, 5, 30, and 200 cycles, respectively), whereas those of the 1:9 and 3:7 bilayer electrodes increased markedly after 200 cycles (from 82.35 to 591.73 Ω and from 114.15 to 289.98 Ω, respectively). These results indicate that the 2:8 bilayer configuration maintained more stable interfacial charge-transfer behavior during repeated cycling. In addition, the shallower slope of the Warburg region at low frequencies indicates sluggish Li^+ diffusion after cycling. In contrast, the 2:8 bilayer electrode maintained a relatively small semicircle and stable Warburg behavior, indicating that the electron transport pathways of the film layer and the efficient Li^+ diffusion pathways of the foam layer were effectively retained even after repeated lithiation/delithiation processes [54].

Figure 5g presents the rate capability of the electrodes at various current densities from 50 to 1000 mA g^{-1}. The single-layer film electrode exhibited a highly consistent capacity within each current density step; however, the overall capacity was low, decreasing from 113.85 mAh g^{-1} at 50 mA g^{-1} to 14.01 mAh g^{-1} at 1000 mA g^{-1}. This is because the compact film structure provides robust mechanical stability and a continuous electron transport pathway, whereas its densely stacked MXene sheets restrict Li^+ diffusion and thus limit the number of accessible active sites [34]. The single-layer foam electrode exhibited a high delithiation capacity of 233.8 mAh g^{-1} at 50 mA g^{-1}, but its capacity significantly decreased to 31.3 mAh g^{-1} at 1000 mA g^{-1}. This suggests that the abundant TiO_2/TiO_x content and the porous structure facilitating Li^+ diffusion pathways enable large capacity at low current density, whereas the limited mechanical robustness of the porous foam structure leads to a sharp capacity decay under high-rate conditions [35]. In contrast, all bilayer electrodes exhibited higher initial capacities and better capacity retention at high current densities than the single-layer film and foam electrodes. Among these, the 2:8 bilayer electrode delivered the highest capacity of 239.94 mAh g^{-1} at 50 mA g^{-1} and maintained 83.24 mAh g^{-1} even at 1000 mA g^{-1}. These results demonstrate that the 2:8 bilayer structure provides the most balanced integration of electron transport and structural integrity through the film layer and Li^+ diffusion and storage through the foam layer, thereby retaining the electrode architecture and charge transport pathways even under high-rate conditions.

Figure 5h further compares the cycling performance of the electrodes for 200 cycles at 50 mA g^{-1}. Consistent with the rate capability results, the single-layer film electrode delivered a limited but highly reversible capacity, decreasing only slightly from 87.21 to 65.41 mAh g^{-1} (75% retention) after 200 cycles, whereas the single-layer foam electrode delivered a higher initial capacity of 250.92 mAh g^{-1} but retained only 89.79 mAh g^{-1} (35.78% retention) after 200 cycles. In contrast, the bilayer electrodes generally exhibited superior cycling performance to the single-layer film and foam electrodes, with the 2:8 bilayer electrode retaining the highest delithiation capacity of 195.12 mAh g^{-1} (51.65% retention) after 200 cycles. The 1:9 electrode showed inferior performance due to an insufficient film fraction to form a continuous electron-conducting backbone, while the 3:7 electrode underperformed owing to a reduced foam fraction that limits the Li^+ diffusion pathway, both resulting in lower capacity retention compared with the 2:8 bilayer. This result demonstrates that the 2:8 bilayer architecture successfully combines the structural and electrical stability of the film layer with the high Li^+ accessibility of the foam layer, thereby achieving an optimal balance between high reversible capacity and cycling stability.

In summary, these results confirm that the 2:8 bilayer design, by maintaining efficient charge-transfer kinetics, overcomes the inherent limitations of single-layer MXene architectures to deliver superior reversible capacity, rate capability, and long-term cycling stability.

3.5. Post-Cycling Morphological Evolution and Structural Stability

Figure 6 shows top-view SEM images comparing the surface morphology evolution of the MXene film, foam, and bilayer electrodes before and after cycling. In the case of the bilayer electrode, morphological observations focused on the electrolyte-contacting upper foam layer. Before cycling, the film electrode exhibited a smooth surface with continuously interconnected, wrinkled MXene sheets. In the foam electrode, crystalline particles with sizes up to approximately 1 μm were observed on the surface, suggesting that Ti species on the MXene surface were partially oxidized during thermal treatment in an air atmosphere, forming TiO_2- or TiO_x-related crystalline domains. Similar particles were more densely observed on the bilayer electrode, likely due to the high surface exposure of its foam layer, which facilitates reactions with oxygen [49]. After cycling, the film electrode retained a relatively continuous MXene sheet network, indicating that the film structure substantially preserved its structural integrity. However, localized tearing, minor pore formation, and uneven surface morphology were observed in some regions. This can be attributed to restricted electrolyte penetration and Li^+ transport caused by the compact stacking structure, which concentrates electrochemical reactions in localized regions [34]. The foam electrode exhibited more pronounced cracks and discontinuous surface domains after cycling. Although the porous architecture facilitates efficient Li^+ diffusion, its limited mechanical robustness leads to pore-wall collapse, sheet disconnection, and crack propagation under repeated Li^+ insertion and extraction. This indicates that, despite its high storage capacity, the single-layer foam architecture suffers from limited structural durability compared with the compact film structure [35]. In contrast, the electrolyte-contacting surface of the bilayer electrode exhibited a relatively stable morphology after cycling, with severe cracks, pore formation, and large-scale delamination effectively suppressed compared with those observed in the film and foam electrodes. Furthermore, the cycled bilayer surface displayed uniformly distributed fine grains. Together with the suppressed crack formation discussed above, this may indicate a more uniform surface reaction. This may be attributed to the complementary roles of the film and foam layers. The film layer maintains high structural integrity to provide mechanical support to the foam layer, while the efficient electron and Li^+ transport pathways within the bilayer structure promote homogeneous electrochemical reactions across the bulk electrode, collectively mitigating localized stress concentration and structural degradation during cycling.

The post-cycling SEM results are consistent with the electrochemical performance shown in Figure 5. The superior cycling performance of the 2:8 bilayer electrode is likely related not only to the mechanical support and continuous electron transport pathway provided by the film layer, but also to the facilitated Li^+ diffusion pathway and the additional Li^+ storage sites enabled by the abundant TiO_2/TiO_x active surface of the foam layer. Together, these complementary features contribute to the enhanced electrochemical stability of the bilayer electrode. Because the capacity of MXene is mainly governed by Li^+ insertion/extraction rather than a phase transition, the film:foam mass ratio set during fabrication is not expected to change significantly during cycling, which may allow this combination to be retained over extended cycling and suggests that the MXene film/foam bilayer is a promising self-standing anode architecture for lithium-ion batteries.

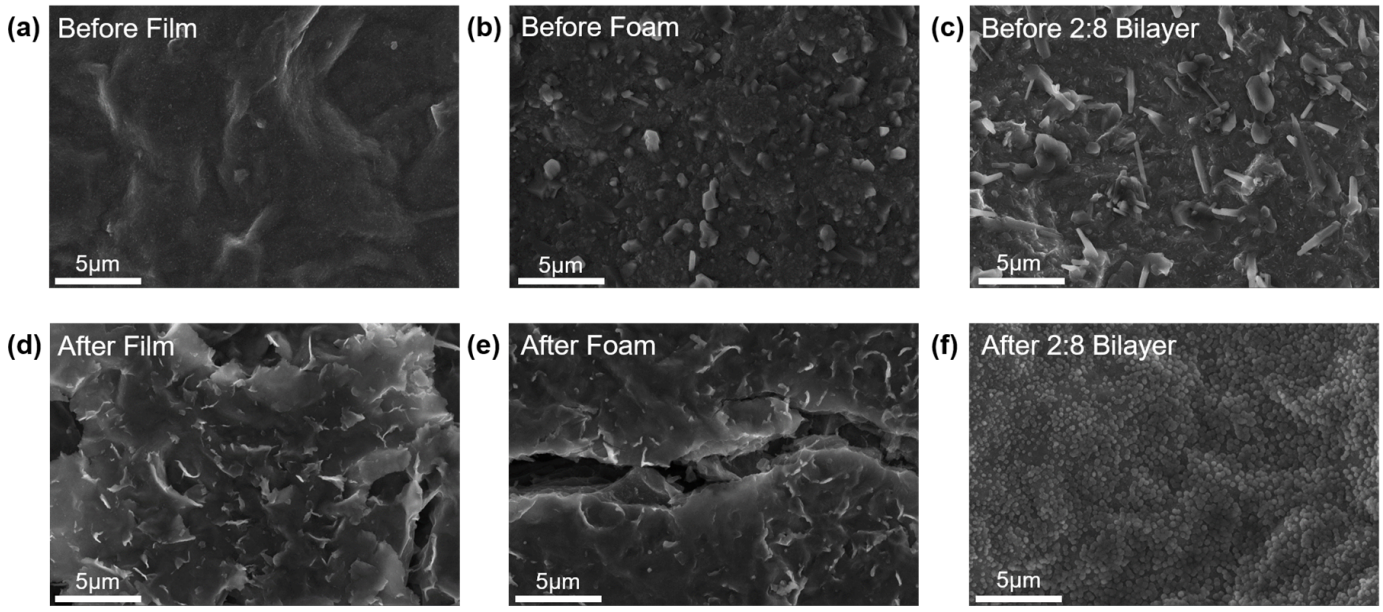


Figure 6. Surface morphology evolution of MXene film, foam, and 2:8 bilayer electrodes before and after cycling. (**a**–**c**) SEM images before cycling and (**d**–**f**) after cycling.

4. Conclusions

In this study, a self-standing $Ti_3C_2T_x$ MXene film/foam bilayer anode was designed to overcome the intrinsic trade-off between the restacking-induced capacity limitation of MXene films and the structural instability of MXene foams. By integrating the structurally robust, electron-conductive film layer with the ion-accessible foam layer, the bilayer architecture achieves highly efficient electron transport and Li^+ diffusion pathways. Furthermore, controlled thermal oxidation introduces a TiO_2/TiO_x-containing active surface, providing abundant Li^+ storage sites within this single self-standing electrode. Kinetic analysis revealed that the 2:8 bilayer electrode exhibits predominantly diffusion-controlled Faradaic redox behavior with low charge-transfer resistance, indicating that Li^+ ions can access active sites throughout the bulk electrode rather than being confined to near-surface regions as in the single-layer architectures. This favorable kinetic behavior translates into a high delithiation capacity of 239.94 mAh g^{-1} at 50 mA g^{-1} and 83.24 mAh g^{-1} at 1000 mA g^{-1}, with recovery to 194.19 mAh g^{-1} upon returning to 50 mA g^{-1}. In addition, the electrode retained a stable capacity of 195.12 mAh g^{-1} at 50 mA g^{-1} after 200 cycles, substantially outperforming the single-layer film and foam electrodes. Post-cycling SEM observations further indicated that the combination of the film and foam layers suppressed the cracking and delamination observed in the single-architecture electrodes, suggesting that structural and electrical continuity was better maintained over extended cycling. These findings demonstrate that rationally combining structurally complementary MXene architectures with in situ surface oxidation offers an effective design principle for overcoming the inherent limitations of self-standing MXene electrodes, providing a broadly applicable strategy for other two-dimensional material-based energy storage systems.

Supplementary Materials: The following supporting information can be downloaded at: https://www.mdpi.com/article/10.3390/batteries12100433/s1, Figure S1: Schematic illustration of the fabrication of self-standing MXene film, foam, and film/foam bilayer electrodes, together with photographs of the fabricated samples and schematic of their electron/Li^+ transport pathways; Figure S2: Photographs of the MXene electrode after electrolyte deposition, showing rapid and complete wetting of the surface, which prevented reliable contact-angle measurement; Figure S3: EDS elemental mapping images of the (a) film, (b) foam, and (c) 2:8 bilayer electrodes, showing the

spatial distributions of C, O, and Ti; Figure S4: Contact-angle images of the 1:9, 2:8, and 3:7 bilayer electrodes; Figure S5: XPS survey spectra of the (a) film and (b) foam electrodes, showing the overall surface elemental composition; Figure S6: (a) Randles–Ševčík plots of anodic and cathodic peak current as a function of the square root of scan rate for the film, foam, and 2:8 bilayer electrodes, and (b) corresponding apparent Li^+ diffusion coefficients; Figure S7: Relative diffusion- and capacitive-controlled contributions of the (a) film and (b) foam electrodes at different scan rates of 0.1, 0.2, 0.5, 1, and 2 mV s^{-1}; Figure S8: Nyquist plots of the film, foam, and bilayer electrodes with different film-to-foam ratios (1:9, 2:8, and 3:7) after (a) 5 and (b) 30 cycles; Figure S9: Comparison of the fitted R_s and R_{ct} values of film, 1:9 bilayer, 2:8 bilayer, 3:7 bilayer, and foam electrodes at 0, 5, 30, and 200 cycles; Table S1: Summary of representative self-standing/binder-free electrode architectures and their reported capacities; Table S2: Phase quantification of anatase and rutile TiO_2 in the film and foam electrodes by Rietveld refinement (Profex/BGMN) of the anatase (101) and rutile (110) reflections; Table S3: Electronic conductivities of film, foam, 2:8 bilayer film plane, and 2:8 bilayer foam plane; Table S4: Relative peak-area fractions obtained from deconvolution of the C 1s, Ti 2p, and O 1s XPS spectra of the film and foam electrodes; Table S5: Elemental compositions of the film and foam electrodes determined by XPS showing the relative contents of Ti, O, C, Al, and F, along with the corresponding O/Ti atomic ratios; Table S6: EIS fitting parameters after 0, 5, 30, and 200 cycles.

Author Contributions: T.H.P.: Writing—original draft, Visualization, Validation, Methodology, Investigation, Formal analysis; K.Y.K.: Writing—original draft, Methodology, Investigation, Formal analysis. J.U.L.: Writing—review and editing, Resources, Supervision, Project administration. Funding acquisition, Conceptualization. All authors have read and agreed to the published version of the manuscript.

Funding: This work was supported by the Energy Technology Policy Development Program (RS-2024-00422897, Development of ultra-high-quality precursors for super premium grade graphite block manufacturing) and the Technology Innovation Program (RS-2026-25531024, Development of High Purity Mesophase Pitch Precursors and Ultra-High-Modulus Pitch-Based Carbon Fibers) funded by the Ministry of Trade, Industry & Energy (MOTIE, Republic of Korea). This research was also supported by the ANCHOR project through the Gyeonggi ANCHOR Center, funded by the Ministry of Education (MOE) and the Gyeonggi-do, Republic of Korea (2026-ANCHOR-09-A07).

Data Availability Statement: Data are contained within the article and Supplementary Materials.

Conflicts of Interest: The authors declare no conflicts of interest. The funders had no role in the design of the study; in the collection, analyses, or interpretation of data; in the writing of the manuscript; or in the decision to publish the results.

References

1. Goodenough, J.B.; Park, K.-S. The Li-ion rechargeable battery: A perspective. *J. Am. Chem. Soc.* **2013**, *135*, 1167–1176. [CrossRef] [PubMed]
2. Armand, M.; Tarascon, J.-M. Building better batteries. *Nature* **2008**, *451*, 652–657. [CrossRef] [PubMed]
3. Moon, J.H.; Lee, S.; Seong, H.; Kim, G.; Jin, Y.; Lee, C.; Ahn, B.H.; Jang, J.Y.; Kwon, S.-R.; Choi, J. Enhanced electrochemical performance of FeSe2@rGO composites as anode materials for lithium-ion batteries. *Carbon Lett.* **2025**, *35*, 3201–3210. [CrossRef]
4. Dunn, B.; Kamath, H.; Tarascon, J.-M. Electrical energy storage for the grid: A battery of choices. *Science* **2011**, *334*, 928–935. [CrossRef] [PubMed]
5. Matsumoto, F.; Fukunishi, M. Review of current collector-, binder-, conductive additive-free, and freestanding electrodes in lithium and related batteries. *Batteries* **2024**, *10*, 330. [CrossRef]
6. Kang, Y.; Deng, C.; Chen, Y.; Liu, X.; Liang, Z.; Li, T.; Hu, Q.; Zhao, Y. Binder-free electrodes and their application for Li-ion batteries. *Nanoscale Res. Lett.* **2020**, *15*, 112. [CrossRef] [PubMed]
7. Hu, L.; Wu, H.; La Mantia, F.; Yang, Y.; Cui, Y. Thin, flexible secondary Li-ion paper batteries. *ACS Nano* **2010**, *4*, 5843–5848. [CrossRef] [PubMed]
8. Hu, B.; Zhou, X.; Xu, J.; Wang, X.; Yuan, N.; Ge, S.; Ding, J. Excellent rate and low temperature performance of lithium-ion batteries based on binder-free $Li_4Ti_5O_{12}$ electrode. *ChemElectroChem* **2020**, *7*, 716–722. [CrossRef]
9. Luo, S.; Wang, K.; Wang, J.; Jiang, K.; Li, Q.; Fan, S. Binder-free $LiCoO_2$/carbon nanotube cathodes for high-performance lithium ion batteries. *Adv. Mater.* **2012**, *24*, 2294–2298. [CrossRef] [PubMed]

10. Wu, Y.; Wu, H.; Luo, S.; Wang, K.; Zhao, F.; Wei, Y.; Liu, P.; Jiang, K.; Wang, J.; Fan, S. Entrapping electrode materials within ultrathin carbon nanotube network for flexible thin film lithium ion batteries. *RSC Adv.* **2014**, *4*, 20010–20016. [CrossRef]
11. Hwang, C.; Song, W.J.; Han, J.G.; Bae, S.; Song, G.; Choi, N.S.; Park, S.; Song, H.K. Foldable electrode architectures based on silver-nanowire-wound or carbon-nanotube-webbed micrometer-scale fibers of polyethylene terephthalate mats for flexible lithium-ion batteries. *Adv. Mater.* **2018**, *30*, 1705445. [CrossRef] [PubMed]
12. Ha, S.H.; Shin, K.H.; Park, H.W.; Lee, Y.J. Flexible lithium-ion batteries with high areal capacity enabled by smart conductive textiles. *Small* **2018**, *14*, 1703418. [CrossRef] [PubMed]
13. Gaikwad, A.M.; Khau, B.V.; Davies, G.; Hertzberg, B.; Steingart, D.A.; Arias, A.C. A high areal capacity flexible lithium-ion battery with a strain-compliant design. *Adv. Energy Mater.* **2015**, *5*, 1401389. [CrossRef]
14. Zhang, C.; Park, S.H.; Seral-Ascaso, A.; Barwich, S.; McEvoy, N.; Boland, C.S.; Coleman, J.N.; Gogotsi, Y.; Nicolosi, V. High capacity silicon anodes enabled by MXene viscous aqueous ink. *Nat. Commun.* **2019**, *10*, 849. [CrossRef] [PubMed]
15. Naguib, M.; Kurtoglu, M.; Presser, V.; Lu, J.; Niu, J.; Heon, M.; Hultman, L.; Gogotsi, Y.; Barsoum, M.W. Two-dimensional nanocrystals produced by exfoliation of Ti_3AlC_2. *Adv. Mater.* **2011**, *23*, 4248–4253. [CrossRef] [PubMed]
16. Naguib, M.; Mashtalir, O.; Carle, J.; Presser, V.; Lu, J.; Hultman, L.; Gogotsi, Y.; Barsoum, M.W. Two-dimensional transition metal carbides. *ACS Nano* **2012**, *6*, 1322–1331. [CrossRef] [PubMed]
17. Subba, C.B.; Rai, D.P.; Tursunov, M.E.; Dekhkonov, A.T.; Pachuau, Z. Comprehensive review of MAX phase and MXene materials: Synthesis, properties, and applications. *Carbon Lett.* **2025**, *35*, 2485–2570. [CrossRef]
18. Anasori, B.; Lukatskaya, M.R.; Gogotsi, Y. 2D metal carbides and nitrides (MXenes) for energy storage. *Nat. Rev. Mater.* **2017**, *2*, 16098. [CrossRef]
19. Gogotsi, Y.; Anasori, B. The rise of MXenes. *ACS Nano* **2019**, *13*, 8491–8494. [CrossRef] [PubMed]
20. Ghidiu, M.; Lukatskaya, M.R.; Zhao, M.-Q.; Gogotsi, Y.; Barsoum, M.W. Conductive two-dimensional titanium carbide 'clay' with high volumetric capacitance. *Nature* **2014**, *516*, 78–81. [CrossRef] [PubMed]
21. Mashtalir, O.; Naguib, M.; Mochalin, V.N.; Dall'Agnese, Y.; Heon, M.; Barsoum, M.W.; Gogotsi, Y. Intercalation and delamination of layered carbides and carbonitrides. *Nat. Commun.* **2013**, *4*, 1716. [CrossRef] [PubMed]
22. Lukatskaya, M.R.; Mashtalir, O.; Ren, C.E.; Dall'Agnese, Y.; Rozier, P.; Taberna, P.L.; Naguib, M.; Simon, P.; Barsoum, M.W.; Gogotsi, Y. Cation intercalation and high volumetric capacitance of two-dimensional titanium carbide. *Science* **2013**, *341*, 1502–1505. [CrossRef] [PubMed]
23. Tang, Q.; Zhou, Z.; Shen, P. Are MXenes promising anode materials for Li ion batteries? Computational studies on electronic properties and Li storage capability of Ti_3C_2 and $Ti_3C_2X_2$ (X = F, OH) monolayer. *J. Am. Chem. Soc.* **2012**, *134*, 16909–16916. [CrossRef] [PubMed]
24. Sun, D.; Wang, M.; Li, Z.; Fan, G.; Fan, L.-Z.; Zhou, A. Two-dimensional Ti_3C_2 as anode material for Li-ion batteries. *Electrochem. Commun.* **2014**, *47*, 80–83. [CrossRef]
25. Er, D.; Li, J.; Naguib, M.; Gogotsi, Y.; Shenoy, V.B. Ti_3C_2 MXene as a high capacity electrode material for metal (Li, Na, K, Ca) ion batteries. *ACS Appl. Mater. Interfaces* **2014**, *6*, 11173–11179. [CrossRef] [PubMed]
26. Koriukina, T.; Kotronia, A.; Halim, J.; Hahlin, M.; Rosen, J.; Edstrom, K.; Nyholm, L. On the use of Ti_3C_2Tx MXene as a negative electrode material for lithium-ion batteries. *ACS Omega* **2022**, *7*, 41696–41710. [CrossRef] [PubMed]
27. Abbasi, F.; Boorboor Ajdari, F.; Mansournia, M.; Asghari, P.; Molaei Aghdam, A. Toward high energy and durable anodes: Critical review on $Li_4Ti_5O_{12}$–MXene composites. *Carbon Lett.* **2025**, *35*, 515–537. [CrossRef]
28. Zhao, M.-Q.; Ren, C.E.; Ling, Z.; Lukatskaya, M.R.; Zhang, C.; Van Aken, K.L.; Barsoum, M.W.; Gogotsi, Y. Flexible MXene/carbon nanotube composite paper with high volumetric capacitance. *Adv. Mater.* **2015**, *27*, 339–345. [CrossRef] [PubMed]
29. Jung, J.Y.; Kim, D.G.; Jung, S.; Kim, S.; Kang, J.Y.; Park, Y.S.; Kim, H.; Kim, N.D.; Kim, P. Water-oxidized and ball-milled reduced graphene oxide based self-supporting electrodes for high performance flexible supercapacitors. *Carbon Lett.* **2025**, *35*, 2729–2740. [CrossRef]
30. Ren, C.E.; Zhao, M.Q.; Makaryan, T.; Halim, J.; Boota, M.; Kota, S.; Anasori, B.; Barsoum, M.W.; Gogotsi, Y. Porous two-dimensional transition metal carbide (MXene) flakes for high-performance Li-ion storage. *ChemElectroChem* **2016**, *3*, 689–693. [CrossRef]
31. Bindhu, D.; Gayathri, M.S.; Ramachandran, A.; Jinchu, I.; Jose, R.; Sreekala, C.O. Bridging the gap: Challenges and industrial translation of MXene/biomass-carbon supercapacitors. *Carbon Lett.* **2026**, *36*, 2041–2065. [CrossRef]
32. Zhao, Q.; Zhu, Q.; Miao, J.; Zhang, P.; Wan, P.; He, L.; Xu, B. Flexible 3D porous MXene foam for high-performance lithium-ion batteries. *Small* **2019**, *15*, 1904293. [CrossRef] [PubMed]
33. Luo, J.; Zhang, W.; Yuan, H.; Jin, C.; Zhang, L.; Huang, H.; Liang, C.; Xia, Y.; Zhang, J.; Gan, Y. Pillared structure design of MXene with ultralarge interlayer spacing for high-performance lithium-ion capacitors. *ACS Nano* **2017**, *11*, 2459–2469. [CrossRef] [PubMed]
34. Sun, N.; Guan, Z.; Zhu, Q.; Anasori, B.; Gogotsi, Y.; Xu, B. Enhanced ionic accessibility of flexible MXene electrodes produced by natural sedimentation. *Nano-Micro Lett.* **2020**, *12*, 89. [CrossRef] [PubMed]

35. Fan, Z.; Wang, Y.; Xie, Z.; Wang, D.; Yuan, Y.; Kang, H.; Su, B.; Cheng, Z.; Liu, Y. Modified MXene/holey graphene films for advanced supercapacitor electrodes with superior energy storage. *Adv. Sci.* **2018**, *5*, 1800750. [CrossRef] [PubMed]
36. Shamsabadi, A.A.; Fang, H.; Zhang, D.; Thakur, A.; Chen, C.Y.; Zhang, A.; Wang, H.; Anasori, B.; Soroush, M.; Gogotsi, Y. The evolution of MXenes conductivity and optical properties upon heating in air. *Small Methods* **2023**, *7*, 2300568. [CrossRef] [PubMed]
37. Hu, S.; Li, S.; Xu, W.; Zhang, J.; Zhou, Y.; Cheng, Z. Rapid preparation, thermal stability and electromagnetic interference shielding properties of two-dimensional Ti_3C_2 MXene. *Ceram. Int.* **2019**, *45*, 19902–19909. [CrossRef]
38. Seredych, M.; Shuck, C.E.; Pinto, D.; Alhabeb, M.; Precetti, E.; Deysher, G.; Anasori, B.; Kurra, N.; Gogotsi, Y. High-temperature behavior and surface chemistry of carbide MXenes studied by thermal analysis. *Chem. Mater.* **2019**, *31*, 3324–3332. [CrossRef]
39. Hart, J.L.; Hantanasirisakul, K.; Lang, A.C.; Anasori, B.; Pinto, D.; Pivak, Y.; Van Omme, J.T.; May, S.J.; Gogotsi, Y.; Taheri, M.L. Control of MXenes' electronic properties through termination and intercalation. *Nat. Commun.* **2019**, *10*, 522. [CrossRef] [PubMed]
40. Liu, N.; Li, Q.; Wan, H.; Chang, L.; Wang, H.; Fang, J.; Ding, T.; Wen, Q.; Zhou, L.; Xiao, X. High-temperature stability in air of $Ti_3C_2T_x$ MXene-based composite with extracted bentonite. *Nat. Commun.* **2022**, *13*, 5551. [CrossRef] [PubMed]
41. Usholihah, N.; Luthfiyah, I.; Meevasana, W.; Pujiarti, H.; Aripriharta, A.; Maaza, M.; Subhan, M.; Diantoro, M. Controlled thermal oxidation of TiO_2-MXene: A scalable annealing strategy for high-performance asymmetric supercapatteries. *Trends Sci.* **2026**, *23*, 12134. [CrossRef]
42. Zhang, T.; Pan, L.; Tang, H.; Du, F.; Guo, Y.; Qiu, T.; Yang, J. Synthesis of two-dimensional Ti_3C_2Tx MXene using HCl+LiF etchant: Enhanced exfoliation and delamination. *J. Alloys Compd.* **2017**, *695*, 818–826. [CrossRef]
43. Brunauer, S.; Emmett, P.H.; Teller, E. Adsorption of gases in multimolecular layers. *J. Am. Chem. Soc.* **1938**, *60*, 309–319. [CrossRef]
44. Zhang, Y.; Mu, Z.; Lai, J.; Chao, Y.; Yang, Y.; Zhou, P.; Li, Y.; Yang, W.; Xia, Z.; Guo, S. MXene/Si@SiOx@C layer-by-layer superstructure with autoadjustable function for superior stable lithium storage. *ACS Nano* **2019**, *13*, 2167–2175. [CrossRef] [PubMed]
45. Liu, H.; Zhang, X.; Zhu, Y.; Cao, B.; Zhu, Q.; Zhang, P.; Xu, B.; Wu, F.; Chen, R. Electrostatic self-assembly of 0D-2D SnO_2 quantum dots/$Ti_3C_2T_x$ MXene hybrids as anode for lithium-ion batteries. *Nano-Micro Lett.* **2019**, *11*, 65. [CrossRef] [PubMed]
46. Slot, T.K.; Yue, F.; Xu, H.; Ramos-Fernandez, E.V.; Sepulveda-Escribano, A.; Sofer, Z.; Rothenberg, G.; Shiju, N.R. Surface oxidation of Ti_3C_2Tx enhances the catalytic activity of supported platinum nanoparticles in ammonia borane hydrolysis. *2D Mater.* **2021**, *8*, 015001. [CrossRef]
47. Yu, J.; Zeng, M.; Zhou, J.; Chen, H.; Cong, G.; Liu, H.; Ji, M.; Zhu, C.; Xu, J. A one-pot synthesis of nitrogen doped porous MXene/TiO2 heterogeneous film for high-performance flexible energy storage. *Chem. Eng. J.* **2021**, *426*, 130765. [CrossRef]
48. Ding, Y.; Zhang, H.; Liu, R.; Wang, Y.; Zheng, Y. Janus-wettability electrode with porous PVA-PDMS interface for enhanced ion transport and high-performance supercapacitor. *Carbon Lett.* **2025**, *35*, 2067–2079. [CrossRef]
49. Gao, J.; Xuan, X.; Tang, Y.; Xie, Y.; Bi, Z.; Zou, J.; Li, L.; Yang, C. Thermal stability of MXene: Current status and future perspectives. *Small* **2025**, *21*, e05881. [CrossRef] [PubMed]
50. Li, A.; Wang, X.; Chen, J.; Dong, C.; Wang, D.; Mao, Z. Surface-termination groups' tuning to improve the lithium-ion-storage performance of Ti_3C_2Tx MXene. *Coatings* **2022**, *12*, 1005. [CrossRef]
51. Yudha SY, M.B.; Halim, M.N.R.; Rifai, A.; Pambudi, F.I. Morphological and electrochemical properties of ZIF-8/biomass-activated carbon hybrids for the anode of lithium-ion battery. *Carbon Lett.* **2026**, *36*, 1927–1942. [CrossRef]
52. Kim, T.; Choi, W.; Shin, H.-C.; Choi, J.-Y.; Kim, J.M.; Park, M.S.; Yoon, W.-S. Applications of voltammetry in lithium ion battery research. *J. Electrochem. Sci. Technol.* **2020**, *11*, 14–25. [CrossRef]
53. Deng, C.; Pan, K.; Zhang, X.; Lai, F.; Yang, G.; Guo, J. Expanded graphite-confined bimetallic sulfide heterostructure enables high-capacity and long-life lithium-ion batteries. *Carbon Lett.* **2025**, *35*, 2981–2991. [CrossRef]
54. Santa-Cruz, L.A.; Tavares, F.C.; Loguercio, L.F.; Dos Santos, C.I.; Galvão, R.A.; Alves, O.A.; Oliveira, M.Z.; Torresi, R.M.; Machado, G. Electrochemical impedance spectroscopy: From breakthroughs to functional utility in supercapacitors and batteries–a comprehensive assessment. *Phys. Chem. Chem. Phys.* **2024**, *26*, 25748–25761. [CrossRef] [PubMed]

Disclaimer/Publisher's Note: The statements, opinions and data contained in all publications are solely those of the individual author(s) and contributor(s) and not of MDPI and/or the editor(s). MDPI and/or the editor(s) disclaim responsibility for any injury to people or property resulting from any ideas, methods, instructions or products referred to in the content.